Monitoring glacier albedo as a proxy to derive summer and annual surface mass balances from optical remote-sensing data

Lucas Davaze[1], Antoine Rabatel[1], Yves Arnaud[1], Pascal Sirguey[2], Delphine Six[1], Anne Letreguilly[1], Marie Dumont[3]

[1] Université Grenoble Alpes, CNRS, IRD, Grenoble INP, IGE (UMR5001), F- 38000 Grenoble, France

[2] National School of Surveying, University of Otago, Dunedin, New Zealand

[3] Météo France, CNRS, CNRM – UMR3589, CEN, F-38000 Grenoble, France

Correspondence to: L. Davaze (lucas.davaze@univ-grenoble-alpes.fr)

Abstract.

Less than 0.25% of the 250,000 glaciers inventoried in the Randolph Glacier Inventory (RGI V.5) are currently monitored with in situ measurements of surface mass balance. Increasing this archive is very challenging, especially using time-consuming methods based on in situ measurements, and complementary methods are required to quantify the surface mass balance of unmonitored glaciers. The current study relies on the so-called albedo method, based on the analysis of albedo maps retrieved from optical satellite imagery acquired since 2000 by the MODIS sensor, onboard of TERRA satellite. Recent studies revealed substantial relationships between summer minimum glacier-wide surface albedo and annual surface mass balance, because this minimum surface albedo is directly related to the accumulation-area ratio and the equilibrium-line altitude.

On the basis of 30 glaciers located in the French Alps where annual surface mass balance are available, our study conducted on the period 2000-2015 confirms the robustness and reliability of the relationship between the summer minimum surface albedo and the annual surface mass balance. For the ablation season, the integrated summer surface albedo is significantly correlated with the summer surface mass balance of the six glaciers seasonally monitored. These results are promising to monitor both annual and summer glacier-wide surface mass balances of individual glaciers at a regional scale using optical satellite images. A sensitivity study on the computed cloud masks revealed a high confidence in the retrieved albedo maps, restricting the number of omission errors. Albedo retrieval artifacts have been detected for topographically incised glaciers, highlighting limitations in the shadows correction algorithm, although inter-annual comparisons are not affected by systematic errors.

41 **1 Introduction**

42 Mountain glaciers represent only 3% of the ice volume on the Earth but contribute
43 significantly to sea level rise (e.g. Church et al., 2013; Gardner et al., 2013; Jacob et al., 2012).
44 In addition, millions of people partly rely on glaciers, either for drinking water, agriculture or
45 related glacier hazards (Baraer et al., 2012; Chen and Ohmura, 1990; Immerzeel et al., 2010;
46 Kaser et al., 2010; Sorg et al., 2012; Soruco et al., 2015). The surface mass balance (SMB) of
47 glaciers is directly driven by the climate conditions; consequently, glaciers are among the most
48 visible proxies of climate change (Dyurgerov and Meier, 2000; Haeberli and Beniston, 1998;
49 Oerlemans, 2001; Stocker et al., 2013). Measuring and reconstructing glacier SMB therefore
50 provides critical insights on climate change both at global and regional scales (Oerlemans,
51 1994).

52 Systematic SMB monitoring programs began in the late 1940s - early 1950s in most of the
53 European countries (e.g., France, Norway, Sweden, Switzerland). Gradually, more glaciers
54 have become monitored, reaching the present worldwide figure of 440. However, this
55 represents only a small sample of the nearly 250,000 inventoried glaciers worldwide (Pfeffer
56 et al., 2014). Among the existing methods to quantify changes in glacier SMB, the well-
57 established glaciological method has become a standard widely used worldwide yielding most
58 of the reference datasets (World Glacier Monitoring Service, WGMS, Zemp et al., 2015).
59 Based on repeated in situ measurements, this method requires intensive fieldwork. This
60 method is however unable to reconstruct SMB of unmonitored glaciers. The Global Terrestrial
61 Network for Glaciers (GTN-G) aims at increasing substantially the number of monitored
62 glaciers to study regional climate signal through changes in SMB. To reach this objective, the
63 development of methods complementary to the ground-based glaciological method is therefore
64 required. Since the 1970s, several methods have taken advantage of satellite imaging to
65 compute changes in glacier volume (Kääb et al., 2005; Rabatel et al., 2017; Racoviteanu et al.,
66 2008). Several glacier surface properties have thus been used as proxies for volume
67 fluctuations: changes in surface elevation from differencing digital elevation models (DEM)

(e.g. Belart et al., 2017; Berthier et al., 2016; Gardelle et al., 2013; Ragettli et al., 2016; Shean et al., 2016); end-of-summer snow line elevation from high spatial resolution optical images (Braithwaite, 1984; Chinn et al., 2005; Meier and Post, 1962; Mernild et al., 2013; Rabatel et al., 2005, 2008, 2016; Shea et al., 2013); mean regional altitude of snow from low spatial resolution optical images (Chaponniere et al., 2005; Drolon et al., 2016); or changes in the glacier surface albedo from high temporal resolution images (Brun et al., 2015; Dumont et al., 2012; Greuell, W. et al., 2007; Greuell and Knap, 2000; Shea et al., 2013; Sirguey et al., 2016). Widely used over icecaps or large ice masses, satellite derived DEM could not yet be confidently used to compute annual or seasonal SMB of mountain glaciers, even if recent studies have revealed promising results for determining SMB changes of large mountainous glacierized areas (Belart et al., 2017; Ragettli et al., 2016). The method based on the correlation between the regional snow cover and glacier SMB have shown satisfying results to retrieve seasonal SMB, especially for the winter period. This method allowed the quantification of 55 glaciers SMB in the European Alps over the period 1998-2014 (Drolon et al., 2016). The method based on the identification on high spatial resolution optical images of the end-of-summer snow line altitude has shown encouraging results in the French Alps, multiplying by six the available long-term annual SMB time series (Rabatel et al., 2016), but need to be automatized to compute glacier SMB at regional scales. In addition, monitoring glacier surface properties on the daily or weekly basis and over large glacierized regions is still challenging with high spatial resolution images. The current study is based on the albedo method used in Dumont et al. (2012), Brun et al. (2015) and Sirguey et al. (2016). Images from the MODerate resolution Imaging Spectroradiometer (MODIS) are processed to compute daily albedo map of 30 glaciers in the French Alps over the period 2000-2015. Then, we rely on the methodological framework proposed by Sirguey et al. (2016) on Brewster Glacier (New-Zealand), looking at the relationships between annual and seasonal SMB and the glacier-wide averaged surface albedo $\overline{\alpha}$. Our overall objective is to study the relationships

between glacier SMB and albedo by: (i) reconstructing the annual albedo cycle for 30 glaciers in the French Alps for the period 2000-2015; (ii) linking the albedo signal to the summer components of the SMB as well as to its annual values for 6 and 30 glaciers, respectively; (iii) assessing the sensitivity of the retrieved albedo towards tuning parameters (cloud coverage threshold for images processing, reliability of detected shadows). Section 2 presents the available SMB datasets used for the comparison and describes briefly the in situ automatic weather stations (AWS) used to assess the quality of MODIS retrieved albedo. The method to retrieve albedo maps is described in Sect. 3. Results are presented and discussed in Sect. 4 and 5. The conclusion gathers the main results of the study and provides perspectives for future works.

2 Study area and data

2.1 Site description

The study focuses on 30 glaciers located in the French Alps (Fig. 1). Each glacier can be classified as mountain glacier, extending over an altitudinal range from around 1600 m a.s.l. (Argentière and Mer de Glace glaciers) to 4028 m a.s.l. (Blanc Glacier), and located between the coordinates: 44°51” N to 46° N and 6°09” E to 7°08” E. The cumulative glacial coverage considered in the present study is 136 km^2, i.e. half of the glacier surface area covered by 593 inventoried glaciers over the French Alps for the period 2006-2009 (Gardent et al., 2014).

Studied glaciers have been selected following four criteria related to the availability of field data and remote sensing constraints, namely: (i) the annual glacier-wide SMB for the study period had to be available; (ii) the glacier surface area had to be wide enough to allow robust multi-pixel analysis; (iii) the glacier had to be predominantly free of debris to allow remotely-sensed observations of the albedo of snow and ice surfaces; and (iv) summer SMB records had to be available to consider summer variability. Finally, 11 glaciers have been selected in the Ecrins range, 14 in Vanoise and 5 in Mont-Blanc (Fig. 1, and listed Table 1).

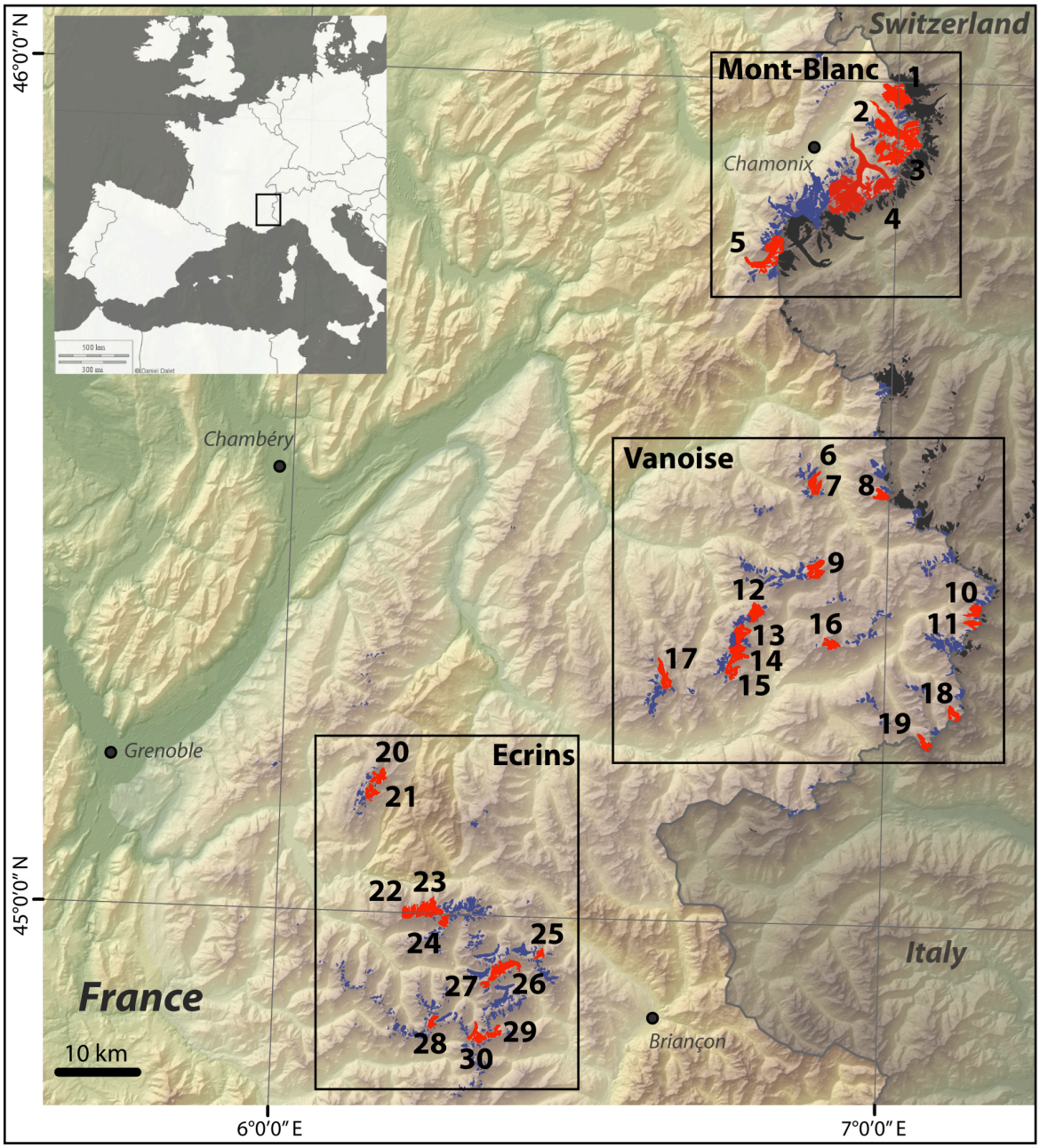

Figure 1 Map of the region of interest with the studied glaciers shown in red (numbers refer to Table 1). The four AWS used in the present study were set up on Saint-Sorlin Glacier (n°20). Adapted from Rabatel et al. (2016).

2.2 MODIS satellite images

The MODIS sensor, onboard the TERRA - EOS/AM-1 satellite is acquiring near-daily images of the Earth since February 25th, 2000. With 36 spectral bands ranging from 0.459 to 14.385 µm, and spatial resolution ranging from 0.25 to 1 km depending on the spectral band, MODIS

is nowadays one of the most used optical sensors for land surface observations. Because of its short temporal revisit time, its long acquisition period and its moderate resolution, images from MODIS are the most suitable for the present work. We therefore rely on about 15,000 MODIS calibrated Level 1B (L1B) swath images.

#	Name	Mask size [Pixel]	$b_a = P_1^a \bar{\alpha}_a^{min} + P_2^a$				$b_s = P_1^s \bar{\alpha}_s^{int} + P_2^b$			
			r^2	$RMSE$	P_1^a	P_2^a	r^2	$RMSE$	P_1^s	P_2^s
1	Tour	71	0.78	0.61	14.9	-7.8				
2	Argentière	111	0.74	0.39	16.8	-8.4	0.76	0.27	12.3	-10.1
3	Talèfre	40	0.46	0.73	17.0	-8.0	0.46	0.69	15.9	-12.1
4	Mer de Glace	246	0.16	0.89	8.7	-5.8	0.69	0.31	15.3	-12.1
5	Tré la Tête	38	0.43	1.25	22.8	-10.0				
6	Savinaz	7	0.23	1.27	12.3	-7.4				
7	Gurraz	17	0.29	0.77	9.8	-5.8				
8	Sassière	19	0.52	0.67	8.2	-4.9				
9	Grande Motte	30	0.83	0.53	13.6	-6.5				
10	Mulinet	18	0.33	0.62	7.7	-4.5				
11	Grand Méan	11	0.44	0.64	7.8	-4.2				
12	Arcelin	37	0.64	0.52	6.6	-3.7				
13	Pelve	44	0.41	0.75	8.7	-5.7				
14	Arpont	41	0.28	1.0	9.8	-5.8				
15	Mahure	20	0.55	0.66	10.1	-5.1				
16	Vallonnet	19	0.36	0.66	3.4	-2.0				
17	Gebroulaz	23	0.62	0.45	9.1	-4.6	0.76	0.28	9.8	-7.9
18	Baounet	11	0.16	0.64	2.8	-2.5				
19	Rochemelon	11	0.31	0.67	4.3	-2.8				
20	Saint-Sorlin	31	0.86	0.37	13.8	-6.3	0.94	0.21	14.7	-11.0
21	Quirlies	15	0.60	0.54	11.4	-5.2				
22	Mont de Lans	35	0.69	0.64	11.4	-5.4				
23	Girose	60	0.70	0.43	9.1	-4.7				
24	Selle	13	0.79	0.41	9.0	-4.4				
25	Casset	7	0.73	0.47	8.9	-4.6				
26	Blanc	44	0.82	0.29	7.9	-3.9	0.72	0.26	9.2	-7.3
27	Vallon Pilatte	7	0.68	0.56	16.0	-7.2				
28	Rouies	14	0.72	0.68	18.0	-7.8				
29	Sélé	12	0.63	0.61	10.9	-5.1				
30	Pilatte	18	0.68	0.83	28.1	-13.1				

Table 1: List of studied glaciers, characteristics and albedo/mass balance correlations over 2000-2015, except for summer coefficients (over 2000-2010). For localization, refer to Fig. 1. Highlighted rows exhibit glaciers where annual and summer in situ glacier-wide SMB data are available. The mask size is expressed in number of pixels. To obtain the glacier mask area in km^2, one should multiply the mask size by 0.0625 km^2. Determination coefficients are expressed for each glacier (full plotted results are shown in supplementary material). Note the units of r^2 (%), *RMSE, P_1 and P_2* (*m w. e.*).

142 **2.3 Surface mass balance data**

143 In the French Alps, six glaciers allow both the summer and annual analyses to be conducted,
144 due to the availability of summer SMB data (b_s) obtained from in situ measurements with the
145 glaciological method (unpublished data, LGGE internal report, listed in Table 1). In addition,
146 glacier-wide annual SMB of the 30 studied glaciers were computed by Rabatel et al. (2016)
147 using the end-of-summer snow line measured on optical remote-sensing images and the
148 glacier-wide mass change quantified from DEMs differencing.

149 For the six glaciers where glacier-wide annual SMB are available from the two methods, i.e.,
150 in situ and satellite measurements, the average of the two estimates was used to calibrate and
151 evaluate the albedo method, in order to derive for each glacier a single relationship SMB *vs.*
152 computed albedo. We did not discuss here the difference in between the considered datasets
153 because these differences have been investigated by Rabatel et al. (2016).

154 **2.4 In situ albedo measurements**

155 Albedo measurements acquired punctually using an AWS on Saint-Sorlin Glacier have been
156 used to evaluate the MODIS retrieved albedo. In situ albedo measurements were available for
157 three periods in the ablation zone (July-August 2006; June-August 2008; June-September
158 2009) and for one period in the accumulation zone (June-September 2008). Albedo data from
159 these AWS have been calculated as the ratio of the reflected to incident shortwave radiation
160 (0.3 to 2.8 μm) using two Kipp and Zonen pyranometers. With a potential tilt of the instrument
161 with respect to surface melting and the intrinsic sensor accuracy (±3%, Six et al., 2009), the
162 calculated albedo at the AWS shows a ±10% accuracy (Kipp and Zonen, 2009; Dumont et al.,
163 2012).

164 **3 Methods**

165 **3.1 MODImLab products**

166 MODIS L1B images were processed using the MODImLab toolbox (Sirguey, 2009). Image
167 fusion between MOD02QKM bands 1 and 2 at 250 m resolution and MOD02HKM bands 3 to
168 7 at 500 m resolution allows 7 spectral bands at 250 m resolution to be produced (Sirguey et

al., 2008). Then, atmospheric and topographic corrections are applied that include multiple reflections due to steep surrounding topography (Sirguey, 2009). Various products are derived from the corrected ground reflectance including snow and ice surface albedo (Dumont et al., 2012). As recommended by Dumont et al. (2012) the WhiteSky (WS) albedo (estimated value of the surface albedo under only diffuse illumination) is considered. The use of an anisotropic reflection model for snow and ice has been preferred to the isotropic case, due to its closer agreement with in situ measurements (Dumont et al., 2012). The MODImLab toolbox also produces sensor geometrical characteristics at the acquisition time such as the solar zenith angle (SZA) and the observation zenith angle (OZA) used for post-processing the images (Sect. 3.4). The MODImLab cloud detection algorithm is more conservative than the original MODIS product (MOD35), and has been preferred as recommended in (Brun et al., 2015).

According to Dumont et al. (2012) and further assessed by (Sirguey et al., 2016) the overall accuracy of MODImLab albedo product under clear-sky conditions is estimated at ±10%.

To mitigate the impact of shadows over the glaciers, MODImLab uses a DEM from the Shuttle Radar Topography Mission (SRTM – 90 m resolution – acquired in 2000) to estimate the sky obstruction by the surrounding topography and to correct the impact of shadows (see Sirguey et al., 2009). The algorithm implemented in MODImLab is fully described in (Sirguey et al., 2009) and inspired from (Dozier et al., 1981; Dozier and Frew, 1990) for the sky obstruction factor processing (Horizon and Vsky in Sirguey et al., 2016), and from (Richter, 1998) for correction of shadows. It is first computed at 125 m resolution, providing Boolean-type products of self and cast shadows per pixel. Results are then averaged and aggregated to 250 m resolution, producing sub-pixel fraction of shadow (further detailed in Sirguey et al., 2009). Finally, MODIS data processed with MODImLab provides, among others, near-daily maps of white-sky albedo at 250 m resolution together with cloud masks and cast and projected shadows.

Albedo maps have been processed for 5,068 images for the Ecrins range, 4,973 for Mont-Blanc and 5,082 for Vanoise over the period 2000-2015. Only images acquired between 09h50

196 and 11h10 AM UTC (+2h in summer for local time conversion) were selected to get minimum
197 SZA and limit projected shadows of surrounding reliefs.

198 **3.2 Glacier masks**

199 Following Dumont et al. (2012) and Brun et al. (2015), we manually created raster masks of
200 the 30 glaciers, based on the glaciers' outlines from 1985-87 (Rabatel et al., 2013) and high
201 spatial resolution (6 m) SPOT-6 images from 2014. All debris-covered areas, together with
202 mixed pixel (rock-snow/ice) have been removed to capture only the snow/ice albedo signal.
203 The resulting number of pixels per glacier is listed in Table 1.

204 **3.3 Surface albedo and glacier-wide mass balance relationship**

205 **3.3.1 Basis of the method**

206 For one glacier in the Alps (Dumont et al., 2012), two in the Himalayas (Brun et al., 2015) and
207 one in the Southern Alps of New Zealand (Sirguey et al., 2016), the summer minimum glacier-
208 wide averaged albedo ($\overline{\alpha}_a^{\min}$) has been significantly correlated to the glacier-wide annual SMB.
209 The relationship between $\overline{\alpha}_a^{\min}$ and glacier-wide SMB results from the fact that solar radiation
210 is the main source of energy for melting snow and ice, both at the surface and within the first
211 centimeters below the surface (Van As, 2011). But this is not sufficient to explain why
212 averaged surface albedo is suitable for monitoring glacier SMB.
213 If we consider a temperate glacier in the mid-latitudes, its surface is fully covered by snow in
214 winter, leading to high and uniform surface albedo ($\overline{\alpha} \approx 0.8$ in Cuffey and Paterson, 2010).
215 During the ablation season, the accumulation area is still covered with snow conversely to the
216 ablation area where the ice is exposed and sometimes covered by debris. The overall albedo of
217 the glacier surface is therefore decreasing over the course of the ablation season, providing
218 information on the ratio of these two areas. The ratio between the size of the accumulation
219 zone and the entire glacier, called the accumulation-area ratio (AAR) has often been used as a
220 predictor of SMB both qualitatively (LaChapelle, 1962; Meier and Post, 1962; Mercer, 1961)
221 or quantitatively (Dyurgerov et al., 2009). Therefore, assessing $\overline{\alpha}_a^{\min}$ provides insights of the

relative share between the exposed ice and the snow-covered areas at the end of the ablation season, also quantified by the AAR.

3.3.2 From annual to summer surface mass balances

In this study, $\overline{\alpha}_a^{\min}$ has been computed for the 30 glaciers in order to validate the method at a regional scale. Only the $\overline{\alpha}_a^{\min}$ occuring in summer have been considered because minimum values out of the summer period are artifacts. Then, $\overline{\alpha}_a^{\min}$ has been directly correlated to available annual SMB data (listed in Table 1).

Following the work by Sirguey et al. (2016) on Brewster Glacier, a similar approach has been used in order to validate the method at a summer scale but only on six glaciers (within our sample of 30) for which the summer SMB are available. Conversely to Sirguey et al. (2016), the summer SMB b_s has been compared to the integrated albedo signal $\overline{\alpha}_s^{\text{int}}$ during the entire ablation season (1st May to 30th September) computed as follow and illustrated in Fig. 2.

$$\overline{\alpha}_s^{\text{int}} = \int_{05.01}^{09.30} \overline{\alpha}(t).dt \qquad \text{Eq. (1)}$$

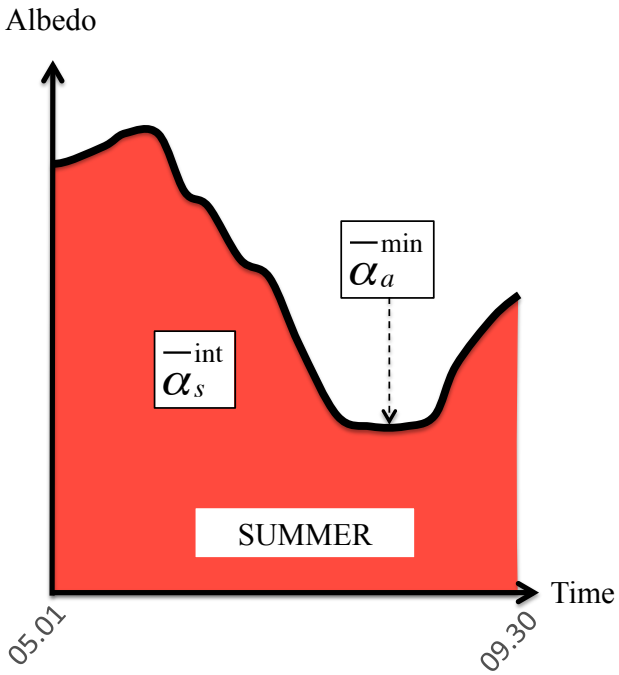

Figure 2: Schematic of a typical albedo cycle over one summer, displaying parameters which have been linked to annual and summer (between 1st May and 30th September in the northern

hemisphere) SMB. $\overline{\alpha}_s^{\text{int}}$ is retrieved using Eq. (1). The summer minimum value of albedo is represented by $\overline{\alpha}_a^{\text{min}}$.

Integrated summer albedos allow to account for snowfall events that can occur during the ablation period (punctual high albedos). As an example, a strong summer snowfall event leading to a rather persistent snow coverage of the glacier will 'feed' the integrated albedo, and physically reduces the glacier melting, which has an impact on the SMB (Oerlemans and Klok, 2004). The method therefore accounts for snowfall events to retrieve the glacier summer SMB. To compare each year together and remove the impact of the variable integration time period for each glacier, $\overline{\alpha}_s^{\text{int}}$ has been divided by the number of integrated days.

3.4 Data filtering

MODIS offers the opportunity to get daily images, but retrieving daily maps of Earth surface albedo remains challenging. Indeed, various sources of error require filtering the available images in order to only capture physical changes of the observed surface and not artifacts. Clouds are known to be a major problem in optical remote sensing of the Earth surface especially in the case of ice and snow covered surfaces. Even if some algorithms exist to differentiate clouds and snow-covered areas (e.g., Ackerman et al., 1998; Sirguey et al., 2009), omission errors are difficult to avoid, leading to erroneous albedo of the surface.

In this study, all images with a presence of cloud greater than 30% of the total glacier surface area have been discarded. This threshold is higher than that chosen in Brun et al. (2015) on the Chhota Shigri Glacier (20%), and we thus discuss Sect. 5.1 the impact of the computed cloud threshold on the derived albedo results. When determining $\overline{\alpha}_a^{\text{min}}$, 0% of cloud cover has been imposed as a condition and visual check for each year and each glacier has been performed. Snapshots from the fusion of MODIS bands 1 to 3 and from bands 4 to 6 (Sirguey et al., 2009) have been used to visually check the images, together with images from other satellites (mostly from the Landsat archive) and pictures and comments from mountaineering forums.

This last step, although laborious meticulous when studying 30 glaciers allowed the identification of the summer minimum to be improved. Visual check of the images also confirms that projected shadows of clouds are not affecting the albedo map. Another source of error is the impact of the OZA. As mentioned in Sirguey et al. (2016), accuracy of the MODIS retrieved albedo strongly decreases for viewing angles above 45° as pixel size increases from 2 to 5-folds from OZA = 45° to 66° (Wolfe et al., 1998). This phenomenon is accentuated when observing steep-sided snow/ice surfaces, surrounded by contrasted surfaces (rocks, forests, lakes...). This distortion could lead to capture the mean albedo of a glacier plus its surroundings. Following this, we decided to filter the images according to their OZA angle, as further described Sect. 4.1.

4 Results

4.1 Retrieved albedo assessment

A quantitative evaluation of the retrieved albedo has been performed with AWS deployed on Saint-Sorlin Glacier. Measurements have been synchronized between punctual albedo for MODIS and a 2-hour averaged albedo around MODIS acquisition time for the AWS. It is worth reminding some differences between the in situ measured albedo data and the one retrieved using MODIS. The downward facing pyranometer stands at around 1 m above the surface, corresponding to a monitored footprint of *ca.* 300 m^2 (theoretical value for a flat terrain) while the pixel area of MODImLab products matches 62,500 m^2. Quantified albedos from each method are therefore not representative of the same area. On the other hand, incoming radiation data are extremely sensitive to a tilt of the sensor located on the AWS and maintaining a constant angle throughout the monitoring period remains challenging, especially during the ablation season. For instance, a tilt of 5° of the pyranometer at the summer solstice can increase by 5% the error on the irradiance measurement (Bogren et al., 2016). No sensor tilt was deployed on the AWS, thus preventing the application of tilt-correction methods (e.g., Wang et al., 2016). Nonetheless, regular visit allowed to maintain the sensor horizontal and to limit errors in the irradiance measurements.

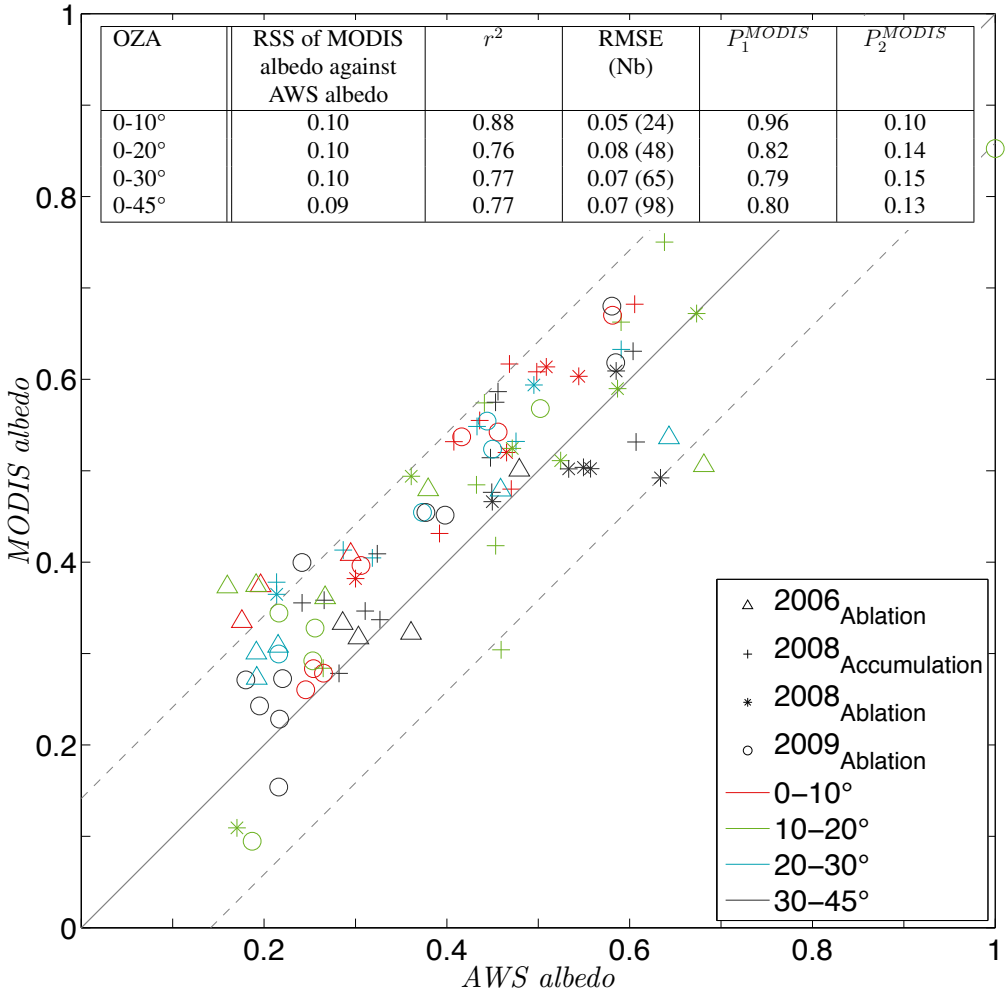

Figure 3: MODIS albedo and AWS albedo data for different OZA classes on Saint-Sorlin Glacier. Years indicated in the caption correspond to the year of acquisition while subscripts express the AWS location in the accumulation or ablation areas. The mean discrepancy between MODIS and AWS albedo per OZA is quantified by the RSS (residual sum of square). Correlation coefficient per OZA classes are also provided, with r^2, RMSE together with the number of compared measurements (Nb), and coefficients of the equation: $MODIS_{albedo} = P_1^{MODIS} AWS_{albedo} + P_2^{MODIS}$. The continuous grey line illustrates the 1:1 relationship between AWS and MODIS retrieved albedo. Thin and dotted lines represent the combined uncertainties on both AWS and MODIS retrieved albedo (absolute value of 10% for each), only accounting for intrinsic sensor accuracy and not for errors related to the acquisition context, e.g. size of the footprint.

Figure 3 illustrates the comparison between the retrieved and measured albedos at the AWS locations for various OZA classes. One can note minor differences between the data plotted in Fig. 3 and those presented in Dumont et al. (2012, Fig. 2). These differences are related to changes in the MODImLab algorithm and different computation of the in situ albedo, integrated over a two-hour period in the current study.

In Fig. 3, the spread between MODIS and AWS albedos is higher for low albedos (i.e. ablation area). This is related to the footprint difference as described earlier, accentuating the albedo differences when monitoring heterogeneous surface (snow patches, melt pounds…), even more pronounced in summer. One can also note that MODIS albedo often over-estimate the AWS albedo value. This over-estimation could be explained by: (1) the MODImLab albedo retrieval algorithm. Indeed, under-estimation of the incoming radiation computed in the MODImLab algorithm would lead to over-estimated retrieved albedo values, in addition the atmospheric corrections used to compute the incident radiation could be hypothesized as source of error (*e.g.* modeled transmittance through a simplified computed atmosphere, refer to (Sirguey et al., 2009) for further description); (2) the AWS albedo measurements. Indeed, view angles of AWS pyranometers (170°) could influence the retrieved albedo by monitoring out-of-glacier features (*e.g.* moraines, rock walls, ...), resulting in under-estimated albedo values. However, it is worth noting that most of the points are within the combined uncertainty of both sensors and these differences in albedo retrieved from MODIS and the AWS are thus hard to interpret.

Finally, Fig. 3 shows substantial differences between OZA<10° and other OZA classes. For OZA<10, MODIS albedos better agree with AWS albedos than for the three other classes. Integrating MODIS images with OZA>10° substantially deteriorate the agreement with AWS albedos (in term of r^2, *RMSE* and the slope P_1^{MODIS}), especially on "narrow" targets as alpine mountain glaciers. We therefore chose to prioritize images acquired with low OZA to avoid

detection of non-glacierized surfaces. Therefore, four classes of images have been selected following the criteria presented in Table 2.

Class	**OZA** (°)	**Criteria**
I	$OZA \leq 10$	All retained
II	$10 < OZA \leq 20$	Retained if more than 7 days between consecutive images from class I
III	$20 < OZA \leq 30$	Retained if more than 7 days between consecutive images from class I+II
IV	$OZA > 30$	Not retained

Table 2: Filtering the images from OZA values.

For the rest of the computation, the absolute ±10% accuracy per pixel estimated in Dumont et al. (2012) has been considered. We determined the uncertainty on $\overline{\alpha}$ by accounting for the spatial variability of the albedo signal within the glacier and considering that our sets of pixels are independent from each other (Eq. (2)):

$$\sigma_{\overline{\alpha}} = \frac{\sigma}{\sqrt{N}} \qquad \text{Eq. (2)}$$

where σ stands for the standard deviation of the pixels albedo with *N* the number of pixels.

4.2 Temporal variability of the albedo signal

Using the "step-by-step" filtering procedure explained in Sect. 3.4, the ~16-yr albedo cycle of each of the 30 glaciers was obtained (results available in the supplementary material). Figure 4 illustrates the entire albedo time series for Saint-Sorlin Glacier over the period 2000-2015. We observed that the albedo decreases from the beginning of summer (dashed red line), reaching $\overline{\alpha}_a^{\min}$ in August/September and rising again at the end of September. This cyclicality is a proxy of surface processes. The snow cover decreases at the beginning of summer until reaching its

lowest extent, and finally increases again with the first snowfall in late summer to reach its maximum extent in winter/spring.

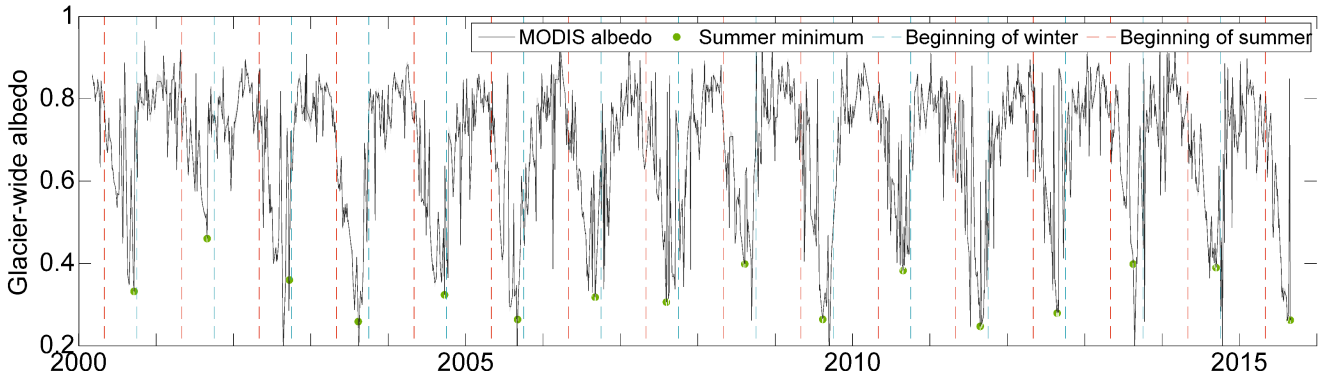

Figure 4: ~16-yr albedo course for Saint-Sorlin Glacier. Glacier-wide averaged albedo is represented with the continuous black line. The green dots spot for each summer the minimum average albedo, and have been manually checked for all years and glaciers. Dashed red and blue lines stand for the beginning of the defined ablation and accumulation seasons (May and October 1st respectively).

The periodicity of the albedo signal is however not so well defined for some of the studied glaciers. For instance, Argentière Glacier exhibits a severe drop of $\overline{\alpha}$ in winter, reaching values as low as summer minimums ($\overline{\alpha} \approx 0.4$). The observed drop of albedo in winter occurs during more than one month centered on the winter solstice (December 21st) and is observed for nine glaciers (Argentière, Baounet, Casset, Blanc, Girose, Pilatte, Vallon Pilatte, Tour and Sélé glaciers, refers to supplementary material for full results). These glaciers are located within the three studied mountain ranges but have the common characteristic to be very incised with steep and high surrounding faces. We studied the albedo series as a function of the SZA to reveal possible shadowing on the observed surfaces. Figure 5 displays the same cycle as Fig. 4 for Argentière Glacier but providing information about SZA. As a reminder, the MODImLab white-sky albedo is independent of the illumination geometry but the computed albedo for each pixel can be subject to shadowing from the surrounding topography.

Two main observations stand out from the winter part of the cycle in Fig. 5: (i) most of MODIS $\overline{\alpha}$ severely decrease under $\overline{\alpha} = 0.6$ for SZA greater than 60° corresponding to November to January images, (ii) these drops are not systematic and we rather observe a dispersion cone than a well-defined bias. As there are no physical meanings to systematic change of the surface albedo during a part of the winter period and owing to the fact that this dispersion is only observed for topographically incised glaciers, these decreases in albedo have been considered as artifacts. These observations led us to perform a sensitivity study on the validity of the shadow mask produced by MODImLab, and to study the impact of these shadows on the retrieved glacier-wide albedo (see 5.2).

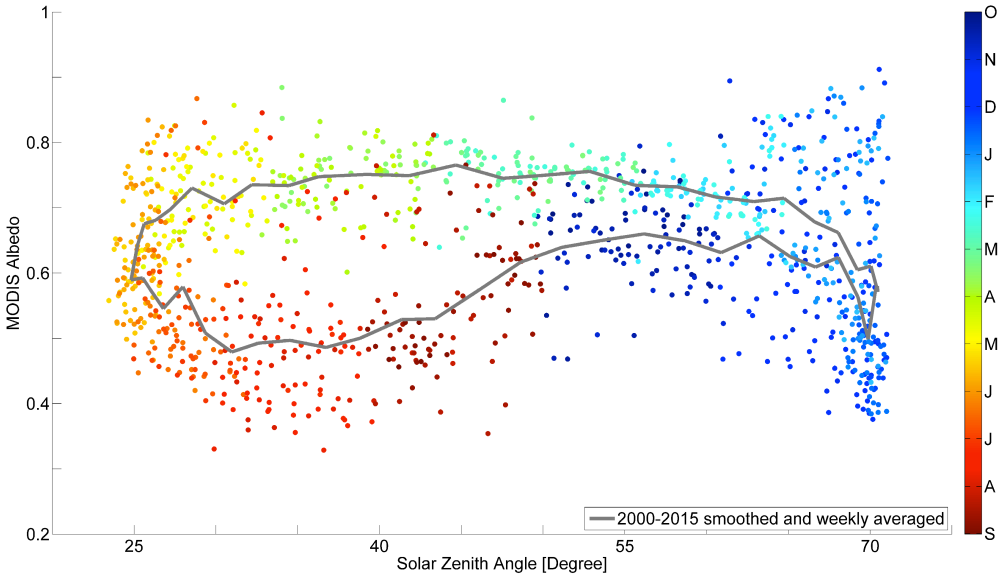

Figure 5: Albedo cycle for Argentière Glacier as a function of the SZA. Each point corresponds to glacier-wide averaged albedo for each available image. The 16 years are displayed. Color scale gives indication on the date of the used image. The thick grey line describes the weekly albedo averaged over the entire study period. For readability purpose, the averaged albedo has been smoothed, using a 7 points running average.

4.3 Albedo and glacier-wide surface mass balance

4.3.1 $\overline{\alpha}_a^{\min}$ and annual surface mass balance

The summer minimum average albedo for each year and each glacier has been linearly correlated to the glacier-wide annual SMB. Figure 6 illustrates the relationship between $\overline{\alpha_a}^{\min}$ and b_a for Blanc Glacier (all the other glaciers are shown in the supplementary material). Error bars result from the dispersion of the SMB dataset for each year, and from the glacier intrinsic variability of the albedo signal the day of $\overline{\alpha_a}^{\min}$ acquisition. For the glaciers where the glacier-wide annual SMB is available from the SLA method, the uncertainty is about ±0.22 *m w.e.* on average (ranging from 0.19 to 0.40 *m w.e.* depending on the glacier, Rabatel et al., 2016).

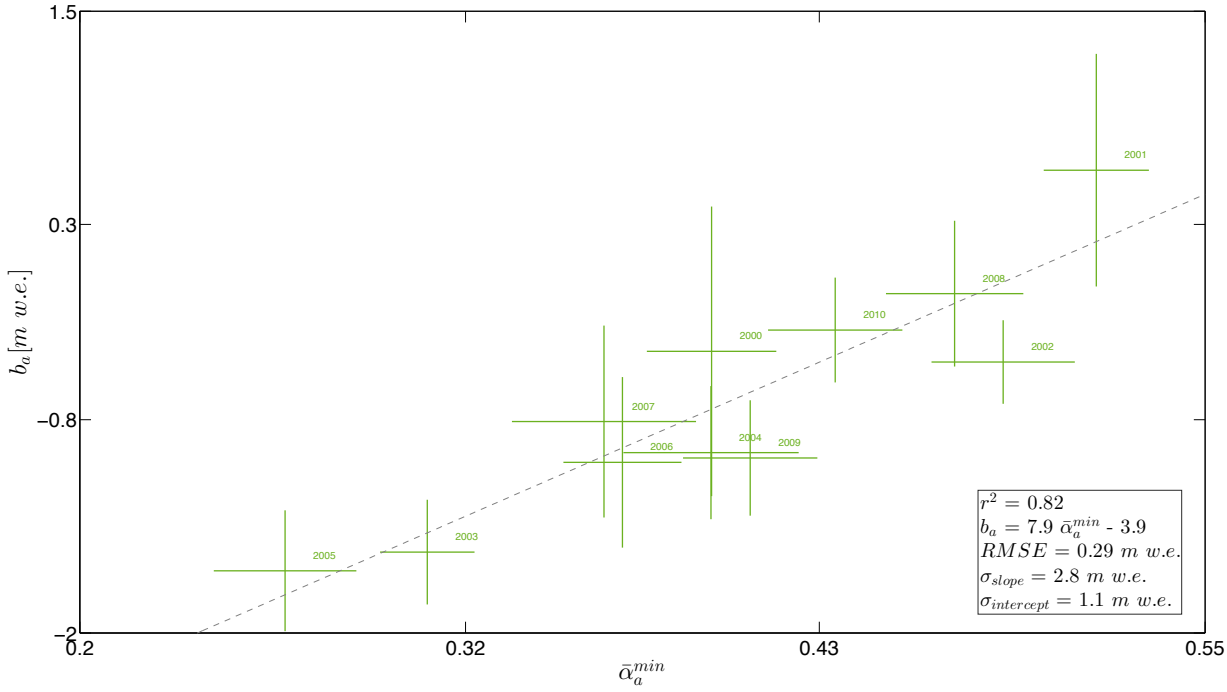

Figure 6: Annual SMB as a function of the MODIS retrieved summer minimum glacier-wide average albedo for Blanc Glacier. Error bars result on the dispersion of the available annual SMB data and on the quadratic sum of the systematic errors made on each albedo measurement. The thin dashed grey line illustrates the line of best fit, along with regression coefficients and significance.

Twenty-seven glaciers show significant correlations (refer to Table 1 for full results) if considering a risk of error of 5% (according to a Student's t test) and confirms the robust correlation between $\overline{\alpha_a}^{\min}$ and b_a. However, the linear correlation has no statistical significance

405 for three glaciers with $r^2 < 0.25$. A possible explanation is the high number of removed images
406 in summer due to manually checked thin overlying clouds not detected by the MODImLab
407 cloud algorithm.
408 Looking at the 27 glaciers for which significant relationships have been found, 2001 is
409 regularly identified as an outlier. According to existing SMB datasets, 2001 is the only year of
410 the period 2000-2015 for which the annual SMB has been positive for all the studied glaciers
411 (+0.80 m w.e. yr^{-1} in average).
412 To predict correctly the surface mass balance values for the year 2001 using the albedo
413 method, monitored minimum glacier-wide average albedo would need to be extremely high
414 (often greater than 0.7, i.e. 0.83 and 0.95 for Rochemelon and Vallonnet glaciers,
415 respectively), to match the regression line derived from other years of the time series (Table
416 1). Taking into consideration snow metamorphism during the summer period, melting at the
417 surface and possible deposition of debris or dusts, monitoring such high albedo values
418 averaged at the glacier scale is unrealistic. As removing 2001 from the time series does not
419 increase the number of glaciers for which the correlation is significant, 2001 has been
420 conserved in the time series. However, this observation reveals a limitation of the albedo
421 method by under-estimating the annual SMB value for years with very positive annual SMB.

422 **4.3.2 $\overline{\alpha_s}^{\text{int}}$ and summer surface mass balance**

423 Studying the integral of the albedo signal during the ablation season can provide insights on
424 the intensity of the ablation season and thus on the summer SMB b_s. As described in Sect.
425 3.3.2, $\overline{\alpha_s}^{\text{int}}$ has been computed and connected to the in situ b_s. Figure 7 illustrates the results
426 for Saint-Sorlin Glacier.

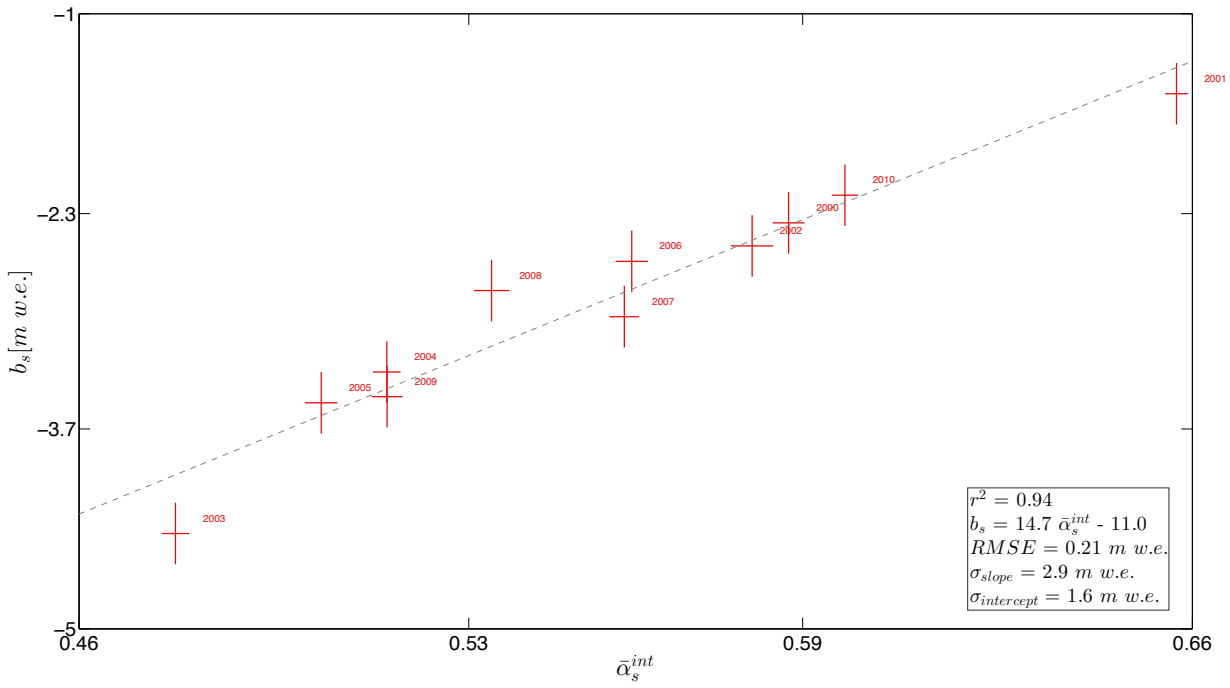

Figure 7: Summer SMB b_s expressed as a function of the integrated albedo over the entire ablation season for Saint-Sorlin Glacier. Error bars result from the uncertainties related to the glaciological method (measurements and interpolation at the glacier scale of the punctual measurements, ±0.20 *m w.e.* in total), and on the quadratic sum of the systematic errors made on each albedo measurement. Thin dashed grey line represents the linear regression showing the best correlation between the two variables, together with correlation coefficients.

Saint-Sorlin Glacier, together with the five other seasonally surveyed glaciers showed a significant correlation between the two observed variables (from $r^2 = 0.46$ to $r^2 = 0.94$ with an error risk < 5%, all statistics referred in Table 1). Conversely to $\bar{\alpha}_a^{min}$, $\bar{\alpha}_s^{int}$ is slightly more robust to the presence of undetected clouds as its value does not rely on a single image. The lowest correlation has been found for Talèfre Glacier. The latter accounts for a relatively large debris-covered tongue that has been excluded when delineating the glacier mask (see supplementary material). Consequently, the low correlation could be partly explained by this missing area, considered in the glaciological method but not remotely sensed. To conclude,

443 $\overline{\alpha_s}^{\text{int}}$ has been significantly correlated to b_s and is therefore a reliable proxy to record the
444 ablation season.
445
446 **5 Discussion**
447 In this section, we first discuss the impact of the threshold applied to the cloud cover fraction
448 on the obtained results. Then, a sensitivity study focused on the algorithm correcting the
449 shadows is presented. We finally express the main limitations and assessments of the albedo
450 method.
451 **5.1 Cloud coverage threshold**
452 As stated in Sect. 3.4, a value of 30% of cloud coverage over the glacier mask has been
453 defined as the acceptable maximum value for considering the albedo map of the day. We
454 computed a sensitivity study on the impact of this threshold on the value of the obtained
455 correlations between the integrated summer albedo and the in situ summer SMB. The summer
456 period has been chosen as it represents the period when the albedo of the glacier is the most
457 contrasted, between bare ice and snow/firn. The glacier-wide average albedo in this period is
458 therefore more sensitive to possible shading of a part of the glacier. Figure 8 illustrates the
459 results for the six seasonally surveyed glaciers. The used value of the allowed cloud coverage
460 appears not to have a substantial impact on the correlation. This observation first implies that
461 the MODImLab cloud product is reliable enough to only compute surface albedo and to avoid
462 too frequent misclassification between the clouds and the surface. It also suggests that
463 removing too many images because of partial cloud cover removes information about the
464 glacier-wide average albedo variability. However, allowing all images, even when the glacier-
465 wide average albedo is computed on only 10% of the glacier (90% of detected cloud
466 coverage), does not reduce significantly the correlation for most of the six glaciers.

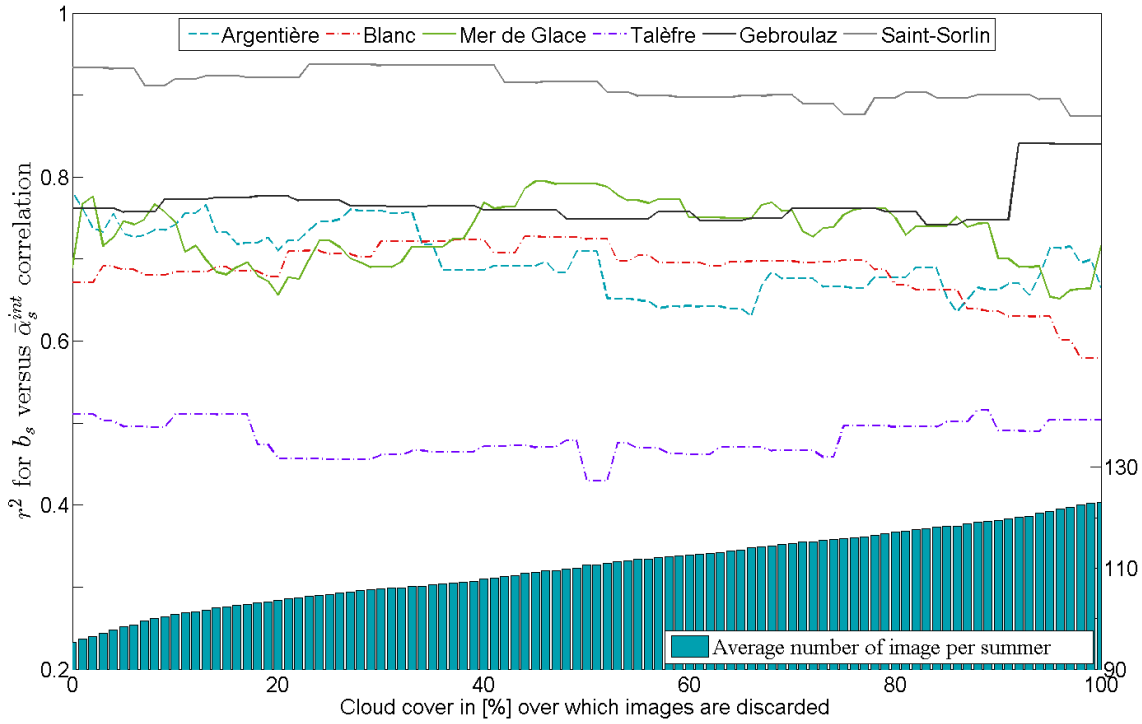

467

468 **Figure 8:** r^2 for the six seasonally surveyed glaciers for the albedo summer integral *versus*
469 summer SMB relationship against the cloud threshold above which images have been
470 discarded during the summer season. For the computation, hundred thresholds have been
471 tested between 0 and 100%. The inner histogram illustrates the number of considered images
472 per summer and averaged on the six glaciers.

473

474 Nevertheless, hypothesizing that the glacier-wide average albedo of a small fraction of the
475 glacier (e.g., 10%) is suitable to represent the entire glacierized surface is questionable. It
476 therefore depends on the size of the observed glacier, where 10% of a glacier of 3 and 30 km^2
477 have not the same meaning, but also on the delineated mask (ablation area not entirely
478 considered because of debris coverage...). The summer-integrated albedo is also highly
479 dependent on the time gap between useful images. In other words, if an image has an
480 "anomalous" glacier-wide average albedo because of high cloud coverage, the impact on the
481 integrated value will be smaller if "normal condition" albedos are monitored at nearby dates.

The average number of available images per year does not largely differ between the various computed cloud coverage thresholds. It varies in average from 95 to 123 images per summer period for respectively 0% and 100% cloud coverage threshold. Intermediate values are 106, 111 and 116 images per summer for 30, 50 and 75% cloud coverage threshold, respectively. The difference in significance of r^2 (according to a Student's t test) between opting for 0% and 100% is almost negligible, and choosing the best cloud threshold value is rather a compromise between the number of used images and the resulting correlation with glacier-wide SMB. We finally concluded that selecting cloud coverage threshold to 30% presents the best determination coefficients between the integrated summer albedo and the summer balance for most of the six glaciers without losing too much temporal resolution.

5.2 Assessment of the impact of shadows on retrieved albedos

In light of the documented dispersion on $\overline{\alpha}$ during some of the winter months on several studied glaciers (Sect. 4.2), sensitivity of the MODIS retrieved albedo against correction of shadows had been assessed. This work has only been conducted on the 250 m resolution raster products and specifically on the cast shadow product because self-shadow corrections can be considered as reliable enough because only related to the DEM accuracy. We thus defined a pixel as "corrected" when at least one of its sub-pixels was classified as shadowed. From then on, two glacier-wide albedos $\overline{\alpha}$ have been defined: (i) $\overline{\alpha}_{\text{non-cor}}$ computed on non-corrected pixels only, classified as non-shadowed; (ii) $\overline{\alpha}$ of both corrected and non-corrected pixels, equal to the glacier-wide average albedo. Figure 9 illustrates the difference between $\overline{\alpha}_{\text{non-cor}}$ and $\overline{\alpha}$ as a function of the percentage of corrected pixels over the entire glacier. The study was performed on Argentière Glacier (111 pixels) that exhibited large $\overline{\alpha}$ artifacts in winter (Fig. 5). The inner diagram allows emphasizing the annual "cycle" of modeled shadows, contrasted between nearly no cast shadows in summer and an almost fully shadowed surface in winter. We represent the 1 standard deviation of $\overline{\alpha}$, averaged by classes of 5% corrected pixels. In other words, it illustrates the mean variability of the glacier-wide surface albedo.

Therefore, for images with $\overline{\alpha}_{\text{non-cor}}$ - $\overline{\alpha}$ within the interval defined by 1 st.dev. of $\overline{\alpha}$, errors resulting from the correction algorithm are smaller than the spatial variability of the glacier-wide albedo glacier. We also selected only significant values, following a normal distribution of the averaged $\overline{\alpha}$. Consequently, only values at ±1σ (68.2%) in term of percentage of corrected pixel have been retained (i.e. when the relative share of corrected pixels ranged from 15.9 to 84.1%). Between 0 and 15.9%, $\overline{\alpha}_{\text{non-cor}}$ and $\overline{\alpha}$ are not sufficiently independent because of low number of corrected pixels, and beyond 84.1%, $\overline{\alpha}_{\text{non-cor}}$ is computed over a too small number of pixels. As a consequence, even if the albedo correction in the shadowed parts of the glacier could be improved, most of the errors related to this correction do not depreciate the results. Above 80% of corrected pixels (December to early February), differences between $\overline{\alpha}_{\text{non-cor}}$ and $\overline{\alpha}$ exceed the monitored spatial variability of $\overline{\alpha}$. These anomalies are at the root of the observed artifacts Fig. 5 by the severe drops of albedos and described Sect. 4.2.

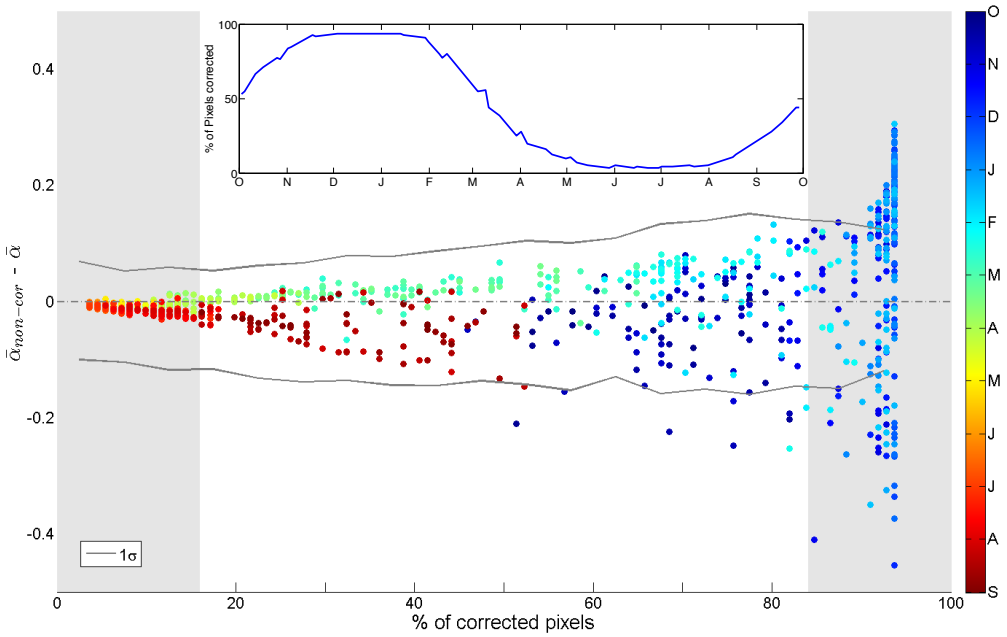

Figure 9: Impact of the ratio of corrected pixels toward the difference between non-corrected and glacier-wide albedo. Each point corresponds to one acquisition and the 16 years are therefore displayed on this graph. Color scale gives indication on the date of the acquired image. Grey shaded areas correspond to ratios of corrected pixels for which $\overline{\alpha}_{\text{non-cor}}$ - $\overline{\alpha}$ has

low statistical robustness (refer to the main text). Thin grey lines represent $1\,\sigma$ standard deviation of $\overline{\alpha}$, averaged by classes of 5% corrected pixels. The inner graph illustrates the amount of corrected pixel, function of the selected month.

In addition, a seasonality in the albedo signal can be observed with $\overline{\alpha}_{\text{non-cor}} - \overline{\alpha} > 0$ in early spring (February to April) while $\overline{\alpha}_{\text{non-cor}} - \overline{\alpha} < 0$ in summer and autumn (June to November). This could be explained by different localizations of shadowed area for a given ratio of corrected pixel. As an example, a glacier could have in October a snow- and shadow-free snout and a covered by fresh snow and shadowed upper section. This configuration would induce a negative difference as we observe from June to November. Conversely, this glacier could present in March (same ratio of corrected pixels than October) a complete snow coverage, leading to a smaller difference between $\overline{\alpha}_{\text{non-cor}}$ and $\overline{\alpha}$ (<0.1) that could even result on positive difference as we observe from February to April.

Finally, observed albedo artifacts in winter are most likely due to the correction of shadows. On the other hand, correcting shadows accurately and consistently is extremely challenging. As illustrated by Fig. 9, a way to confidently consider the albedo signal is to exclude values with too large share of corrected pixels. However, because of the inter-annual approach carried out in this study, such systematic artifact is not depreciating the results but would be a major issue on studies focused on albedo values themselves (e.g. maps of snow extents…).

5.3 Limits of the albedo method

In agreement with Dumont et al. (2012) and Brun et al. (2015), retrieving the glacier annual SMB from albedo summer minimums proves to be an efficient method. Low correlations often result from high and persistent cloud coverage during summer, reducing the chance of spotting the albedo summer minimum. For SMB reconstruction purpose, a future line of research could rest upon linking morpho-topographic features of the glacier such as glacier surface area, mean altitude or slope to the regression coefficients of both annual and seasonal SMB *vs.*

albedo relationships, giving the opportunity to establish analogy between monitored and unmonitored glaciers. Tests have been carried out but no significant and satisfying results have been obtained, due to a presumably too heterogeneous data set, where large glaciers (>10 km^2) and/or south-facing glaciers are largely under-represented. Larger scale studies and multi-variable correlations in between morpho-topographic features could be for instance envisaged. Rabatel et al., (2017) recently proposed an alternative approach to reconstruct the annual mass balance of unmonitored glacier on the basis of the albedo method. This approach relies on the ELA-method (Rabatel et al., 2005), but using the remotely sensed monitored $\overline{\alpha}_a^{\min}$ together with the accumulation area ration (AAR), the glacier hypsometry, and the regional SMB-elevation gradient (which is the annual SMB gradient in the vicinity of the glacier ELA). For an exhaustive description of this approach, refer to Rabatel et al., (2017).

Using the albedo method for the summer period has shown promising results, with significant correlations found for the six seasonally monitored glaciers. There is still in this approach a step to retrieve the summer SMB of an unmonitored glacier with high confidence.

The winter period has also been considered in the framework of this study, but has not been presented in the main body of this publication because of underwhelming results. The albedo signal between 1st October and 30th April has been computed similarly to Sirguey et al. (2016) by integrating the winter albedo signal, only when exceeding a certain threshold $\overline{\alpha}_T$, as described by Eq. (3)):

$$\overline{\alpha}_w^{\text{int}} = \int \overline{\alpha}(t) \begin{cases} \text{if } \overline{\alpha}(t) \text{ is found between 10.01 and 04.30} \\ \text{Only if } \overline{\alpha}(t) \geq \overline{\alpha}_T \end{cases} \quad \text{Eq. (3)}$$

According to Sirguey et al., 2016, the use of $\overline{\alpha}_T$ allows to detect all snowfall events on the glacier, by monitoring abrupt rises of $\overline{\alpha}$. One of the main conclusions of the latter study was the ability of the computed $\overline{\alpha}_w^{\text{int}}$ to monitor the frequency of snowfall events, themselves proxy of the accumulation of snow on the glacier, known to be one of the main component of the winter SMB.

576 $\bar{\alpha}_T$ has been chosen to maximize the correlation between the retrieved cumulative winter
577 albedo $\bar{\alpha}_w^{\text{int}}$ and the winter SMB. Threshold values have been computed independently for each
578 of the six seasonally monitored glaciers. To evaluate the impact of this threshold, $\bar{\alpha}_w^{\text{int}}$ has also
579 been computed without threshold over winter months (equivalent to $\bar{\alpha}_T = 0$). Table 3 gathers
580 all the coefficients obtained from the relationship $\bar{\alpha}_w^{\text{int}}$ *vs.* b_w, with and without the use of an
581 albedo threshold $\bar{\alpha}_T$.

Glacier	$\bar{\alpha}_T$	r^2 **using** $\bar{\alpha}_T$	r^2 **without** $\bar{\alpha}_T$
Saint-Sorlin	0.76	0.75	0.21
Argentière	0.58	0.88	0.76
Talèfre	0.68	0.59	0.25
Mer de Glace	0.53	0.90	0.87
Gebroulaz	0.75	0.36	0.25
Blanc	0.70	0.33	0.21

582

583 **Table 3:** Coefficients of determination for the relationship between the winter SMB b_w and the
584 integrated winter albedo, computed with and without the albedo threshold $\bar{\alpha}_T$.

585 For Argentière and Mer de Glace glaciers, a significant correlation is found whatever the value
586 of the albedo threshold $\bar{\alpha}_T$. For the four other glaciers, using $\bar{\alpha}_T$ largely improves the
587 correlation. However, $\bar{\alpha}_T$ is far from being uniform on the six glaciers ($0.53 \geq \bar{\alpha}_T \geq 0.76$). In
588 addition, for most of the considered glaciers, correlation coefficients abruptly deteriorate when
589 changing this threshold, which does not allow using a "regional" threshold for all considered
590 glaciers. On the other hand, Argentière and Mer de Glace without the use of $\bar{\alpha}_T$ provide the
591 best correlation coefficients compared to the other four glaciers; it is noteworthy that they are
592 by far the largest glaciers of our monitoring set (14.59 and 23.45 km^2 for Argentière and Mer
593 de Glace glaciers, respectively). With a glacier snout reaching 1600 m a.s.l., the tongue of
594 these glaciers can experience melting events (resulting in contrasted pixels in terms of albedo
595 value), even during the winter season. Another difference between our study and Sirguey et al.
596 (2016) is that their work focused only on Brewster glacier, defined as a maritime glacier.

These types of glaciers, even during the accumulation period can experience strong varying albedos in their lower reaches, which leads to similar behaviors in winter as for Argentière and Mer de Glace glaciers. We therefore reconsider the idea of Sirguey et al. (2016) to use a threshold as a representative value of fresh snowfall, as there is no physical reason that this threshold varies, at least within the same region. However, an interesting perspective would be to apply the method without threshold, on a set of other maritime or large glaciers (> 10 km^2).

An additional approach has been carried out, aiming at retrieving b_w by deduction from the reconstructed b_a and b_s from the albedo signal. This approach, not using the winter albedo signal, is poorly correlated (r^2<0.16) to in situ b_w for the six seasonally monitored glaciers. Indeed, the result extremely depends on the quality of the correlations between b_a, b_s and the albedo signals. Saint-Sorlin Glacier is a good example, being one of the glaciers with the highest correlations for the annual (r^2 = 0.86) and summer (r^2 = 0.94) SMB. Subtracting b_s from b_a to computed b_w leads to an average difference between computed and measured b_w of ±0.41 m w.e for the 10 simulated years. As a consequence, in case of low correlations between SMB and albedo, errors in the computed winter SMB become exacerbated.

6 Conclusion

In this study, we used the so-called albedo method to correlate annual and summer SMB to glacier-wide average albedos obtained from MODIS images. This method has been carried on 30 glaciers located in the French Alps, over the period 2000-2015. Images processing has been performed using the MODImLab algorithm, and filters on the images have been applied, removing images with more than 30% cloud coverage, and excluding images with satellite observation angles greater than 30°. Quality assessment has been performed and close agreement has been found between albedos from AWS installed on Saint-Sorlin Glacier and MODIS retrieved albedo values. Annual SMB have been significantly correlated to the summer minimum albedo for 27 of the 30 selected glaciers, confirming this variable as a good proxy of the glacier-wide annual SMB. For the six seasonally monitored glaciers, summer

624 SMBs obtained from the glaciological method have been significantly linked to the integral of
625 the summer albedo. However, calculating the integral of the winter albedo to quantify the
626 winter SMB as done by Sirguey et al. (2016) has shown underwhelming results. Monitoring
627 winter glacier surface albedo may provide good insights on the frequency of snow
628 accumulation at the surface of the glacier but lacks in quantifying the amount of accumulation.
629 Glaciers that experience complete snow coverage during most of the winter season showed the
630 lowest correlation ($r^2 \leq 0.33$) while the two glaciers showing the best correlations are subject
631 to some events of surface melting in their lower reaches. Yet, this approach should not be
632 definitively forsaken but requires improvements to confidently retrieve winter SMB.
633 Sensitivity study on the impact of the considered cloud coverage has revealed a high
634 confidence in the MODImLab cloud algorithm, limiting pixel misclassifications, and a rather
635 high tolerance of the integrated signal to the number of partly cloud-covered images. This
636 confidence on cloud filters is very promising to document unmonitored glaciers. Correction of
637 shadows by the MODImLab algorithm has however revealed some limitations when a large
638 share of the glacier is shadowed by the surrounding topography (around winter solstice).
639 Despite this, severe and artificial drops of albedo in winter have not been identified as an
640 obstacle for monitoring both summer and winter SMB. Such systematic errors are not an issue
641 for inter-annual studies, but would be a serious issue on studies focused on albedo values
642 themselves. For future works, the MODIS archive together with albedo maps, cloud and
643 shadow masks processed with MODImLab, together with validation data from AWS offer a
644 unique dataset to monitor the temporal and spatial evolution of the surface albedo of glaciers
645 at a regional scale. Computing for instance the absorbed solar radiation (Bair et al., 2016) by
646 date and for each glacier would then be an appropriated protocol to estimate the impact of a
647 changing glacier surface albedo in terms of snow or ice melt. Quantifying albedo changes and
648 resulting mass losses with such an approach would be of major interest to better understand
649 the potential effects of possibly increasing dust content, glacier orientation or snow grain
650 growth on glacier surface melt processes.

To conclude, the use of optical satellite images to estimate glacier surface processes and quantify annual and summer SMB from the albedo cycle is very promising and should be expanded to further regions. Using images from different satellites, combining high spatial and temporal resolution instruments, could substantially reduces uncertainties, especially for spotting the albedo summer minimum with more confidence, but also to improve the temporal resolution. This method could then in the short term, become reliable for retrieving SMB of monitored and unmonitored glaciers.

Acknowledgment

This study was conducted within the *Service National d'Observation* GLACIOCLIM. Equipex GEOSUD (*Investissements d'avenir* - ANR-10-EQPX-20) is acknowledged for providing the 2014 SPOT-6 images. The MODIS Level-1B data were processed by the MODIS Adaptive Processing System (MODAPS) and the Goddard Distributed Active Archive Center (DAAC) and are archived and distributed by the Goddard DAAC. In situ mass balance data for the Glacier Blanc were kindly provided by the *Parc National des Ecrins*. The authors acknowledge the contribution the Labex OSUG@2020 (*Investissements d'avenir* – ANR10 LABX56). Pascal Sirguey thanks the University of Grenoble Alpes and Grenoble-INP for the 6-month "invited professor grant" obtained in 2015-16.

REFERENCES

Ackerman, S. A., Strabala, K. I., Menzel, W. P., Frey, R. A., Moeller, C. C. and Gumley, L. E.: Discriminating clear sky from clouds with MODIS, J. Geophys. Res., 103(D24), 32–141, doi:10.1029/1998JD200032, 1998.

Bair, E. H., Rittger, K., Davis, R. E., Painter, T. H. and Dozier, J.: Validating reconstruction of snow water equivalent in California's Sierra Nevada using measurements from the NASAAirborne Snow Observatory, Water Resour. Res., 52(11), 8437–8460, doi:10.1002/2016WR018704, 2016.

Baraer, M., Mark, B. G., Mckenzie, J. M., Condom, T., Bury, J., Huh, K.-I., Portocarrero, C., Gomez, J. and Rathay, S.: Glacier recession and water resources in Peru's Cordillera Blanca, J. Glaciol., 58(207), 134–150, 2012.

Belart, J. M. C., Berthier, E., Magnússon, E., Anderson, L. S., Pálsson, F., Thorsteinsson, T., Howat, I. M., Aðalgeirsdóttir, G., Jóhannesson, T. and Jarosch, A. H.: Winter mass balance of Drangajökull ice cap (NW Iceland) derived from satellite sub-meter stereo images, The Cryosphere, 11(3), 1501–1517, doi:10.5194/tc-11-1501-2017, 2017.

Berthier, E., Cabot, V., Vincent, C. and Six, D.: Decadal Region-Wide and Glacier-Wide Mass Balances Derived from Multi-Temporal ASTER Satellite Digital Elevation Models. Validation over the Mont-Blanc Area, Front. Earth Sci., 4, doi:10.3389/feart.2016.00063, 2016.

Bogren, W. S., Burkhart, J. F. and Kylling, A.: Tilt error in cryospheric surface radiation measurements at high latitudes: a model study, The Cryosphere, 10(2), 613–622, doi:10.5194/tc-10-613-2016, 2016.

Braithwaite, R. J.: Can the Mass Balance of a Glacier be Estimated from its Equilibrium-Line Altitude?, J. Glaciol., 30(106), 364–368, doi:10.1017/S0022143000006237, 1984.

Brun, F., Dumont, M., Wagnon, P., Berthier, E., Azam, M. F., Shea, J. M., Sirguey, P., Rabatel, A. and Ramanathan, A.: Seasonal changes in surface albedo of Himalayan glaciers from MODIS data and links with the annual mass balance, The Cryosphere, 9(1), 341–355, doi:10.5194/tc-9-341-2015, 2015.

Chaponniere, A., Maisongrande, P., Duchemin, B., Hanich, L., Boulet, G., Escadafal, R. and Elouaddat, S.: A combined high and low spatial resolution approach for mapping snow covered areas in the Atlas mountains, Int. J. Remote Sens., 26(13), 2755–2777, 2005.

Chen, J. and Ohmura, A.: Estimation of Alpine glacier water resources and their change since the 1870s, IAHS Publ, 193, 127–135, 1990.

Chinn, T. J., Heydenrych, C. and Salinger, M. J.: Use of the ELA as a practical method of monitoring glacier response to climate in New Zealand's Southern Alps, J. Glaciol., 51(172), 85–95, 2005.

Church, J. A., Clark, P. U., Cazenave, A., Gregory, J. M., Jevrejeva, S., Levermann, A., Merrifield, M., Milne, G., Nerem, R., Nunn, P. and others: Sea level change, Clim. Change 2013 Phys. Sci. Basis Work. Group Contrib. Fifth Assess. Rep. Intergov. Panel Clim. Change, 1137–1216, doi:10.1088/1748-9326/8/1/014051, 2013.

710 Cuffey, K. M. and Paterson, W. S. B.: The Physics of Glaciers, Elsevier Science. [online]
711 Available from: https://books.google.fr/books?id=Jca2v1u1EKEC, 2010.

712 Dozier, J. and Frew, J.: Rapid calculation of terrain parameters for radiation modeling
713 from digital elevation data, IEEE Trans. Geosci. Remote Sens., 28(5), 963–969,
714 doi:10.1109/36.58986, 1990.

715 Dozier, J., Bruno, J. and Downey, P.: A faster solution to the horizon problem, Comput.
716 Geosci., 7, 145–151, doi:10.1016/0098-3004(81)90026-1, 1981.

717 Drolon, V., Maisongrande, P., Berthier, E., Swinnen, E. and Huss, M.: Monitoring of
718 seasonal glacier mass balance over the European Alps using low-resolution optical
719 satellite images, J. Glaciol., 62(235), 912–927, doi:10.1017/jog.2016.78, 2016.

720 Dumont, M., Sirguey, P., Arnaud, Y. and Six, D.: Monitoring spatial and temporal variations
721 of surface albedo on Saint Sorlin Glacier (French Alps) using terrestrial photography,
722 The Cryosphere, 5(3), 759–771, doi:10.5194/tc-5-759-2011, 2011.

723 Dumont, M., Gardelle, J., Sirguey, P., Guillot, A., Six, D., Rabatel, A. and Arnaud, Y.: Linking
724 glacier annual mass balance and glacier albedo retrieved from MODIS data, The
725 Cryosphere, 6(6), 1527–1539, doi:10.5194/tc-6-1527-2012, 2012.

726 Dyurgerov, M., Meier, M. F. and Bahr, D. B.: A new index of glacier area change: a tool for
727 glacier monitoring, J. Glaciol., 55(192), 710–716, doi:10.3189/002214309789471030,
728 2009.

729 Dyurgerov, M. B. and Meier, M. F.: Twentieth century climate change: Evidence from
730 small glaciers, Proc. Natl. Acad. Sci., 97(4), 1406–1411, doi:10.1073/pnas.97.4.1406,
731 2000.

732 Gardelle, J., Berthier, E., Arnaud, Y. and Kääb, A.: Region-wide glacier mass balances over
733 the Pamir-Karakoram-Himalaya during 1999–2011, The Cryosphere, 7(4), 1263–1286,
734 doi:10.5194/tc-7-1263-2013, 2013.

735 Gardent, M., Rabatel, A., Dedieu, J.-P. and Deline, P.: Multitemporal glacier inventory of
736 the French Alps from the late 1960s to the late 2000s, Glob. Planet. Change, 120, 24–37,
737 doi:10.1016/j.gloplacha.2014.05.004, 2014.

738 Gardner, A. S., Moholdt, G., Cogley, J. G., Wouters, B., Arendt, A. A., Wahr, J., Berthier, E.,
739 Hock, R., Pfeffer, W. T., Kaser, G., Ligtenberg, S. R. M., Bolch, T., Sharp, M. J., Hagen, J. O.,
740 Broeke, M. R. van den and Paul, F.: A Reconciled Estimate of Glacier Contributions to Sea
741 Level Rise: 2003 to 2009, Science, 340(6134), 852–857, doi:10.1126/science.1234532,
742 2013.

743 Greuell, W. and Knap, W. H.: Remote sensing of the albedo and detection of the slush line
744 on the Greenland ice sheet, J. Geophys. Res. Atmospheres, 105(D12), 15567–15576,
745 2000.

746 Greuell, W., Kohler, J., Obleitner, F., Glowacki, P., Melvold, K., Bernsen, E. and Oerlemans,
747 J.: Assessment of interannual variations in the surface mass balance of 18 Svalbard
748 glaciers from the Moderate Resolution Imaging Spectroradiometer/Terra albedo
749 product, J. Geophys. Res. Atmospheres, 112, D07105/1null, 2007.

Haeberli, W. and Beniston, M.: Climate Change and Its Impacts on Glaciers and Permafrost in the Alps, Ambio, 27(4), 258–265, 1998.

Immerzeel, W. W., Beek, L. P. H. van and Bierkens, M. F. P.: Climate Change Will Affect the Asian Water Towers, Science, 328(5984), 1382–1385, doi:10.1126/science.1183188, 2010.

Jacob, T., Wahr, J., Pfeffer, W. T. and Swenson, S.: Recent contributions of glaciers and ice caps to sea level rise, Nature, 482(7386), 514–518, doi:10.1038/nature10847, 2012.

Kääb, A., Huggel, C., Fischer, L., Guex, S., Paul, F., Roer, I., Salzmann, N., Schlaefli, S., Schmutz, K., Schneider, D., Strozzi, T. and Weidmann, Y.: Remote sensing of glacier- and permafrost-related hazards in high mountains: an overview, Nat Hazards Earth Syst Sci, 5(4), 527–554, doi:10.5194/nhess-5-527-2005, 2005.

Kaser, G., Grosshauser, M. and Marzeion, B.: Contribution potential of glaciers to water availability in different climate regimes, Proc. Natl. Acad. Sci., 107, 20223–20227, doi:10.1073/pnas.1008162107, 2010.

Kipp and Zonen: Instruction Manuel CNR1 Net radiometer, 2009.

LaChapelle, E.: Assessing glacier mass budgets by reconnaissance aerial photography, J. Glaciol., 4, 290–297, 1962.

Meier, M. F. and Post, A.: Recent variations in mass net budgets of glaciers in western North America, IASH Publ, 58, 63–77, 1962.

Mercer, J. H.: The Response of Fjord Glaciers to Changes in the Firn Limit, J. Glaciol., 3(29), 850–858, doi:10.1017/S0022143000027222, 1961.

Mernild, S. H., Pelto, M., Malmros, J. K., Yde, J. C., Knudsen, N. T. and Hanna, E.: Identification of snow ablation rate, ELA, AAR and net mass balance using transient snowline variations on two Arctic glaciers, J. Glaciol., 59(216), 649–659, 2013.

Oerlemans: Glaciers and Climate Change, Balkema. [online] Available from: http://dspace.library.uu.nl/handle/1874/22045 (Accessed 13 July 2017), 2001.

Oerlemans, J.: Quantifying Global Warming from the Retreat of Glaciers, Science, 264(5156), 243–245, 1994.

Oerlemans, J. and Klok, E. J.: Effect of summer snowfall on glacier mass balance, Ann. Glaciol., 38, 97–100, doi:10.3189/172756404781815158, 2004.

Pfeffer, W. T., Arendt, A. A., Bliss, A., Bolch, T., Cogley, J. G., Gardner, A. S., Hagen, J.-O., Hock, R., Kaser, G., Kienholz, C., Miles, E. S., Moholdt, G., Mölg, N., Paul, F., Radić, V., Rastner, P., Raup, B. H., Rich, J. and Sharp, M. J.: The Randolph Glacier Inventory: a globally complete inventory of glaciers, J. Glaciol., 60(221), 537–552, doi:10.3189/2014JoG13J176, 2014.

Rabatel, A., Dedieu, J.-P. and Vincent, C.: Using remote-sensing data to determine equilibrium-line altitude and mass-balance time series: validation on three French glaciers, 1994–2002, J. Glaciol., 51(175), 539–546, doi:10.3189/172756505781829106, 2005.

789 Rabatel, A., Dedieu, J.-P., Thibert, E., Letréguilly, A. and Vincent, C.: 25 years (1981–2005)
790 of equilibrium-line altitude and mass-balance reconstruction on Glacier Blanc, French
791 Alps, using remote-sensing methods and meteorological data, J. Glaciol., 54(185), 307–
792 314, doi:10.3189/002214308784886063, 2008.

793 Rabatel, A., Letréguilly, A., Dedieu, J.-P. and Eckert, N.: Changes in glacier equilibrium-line
794 altitude in the western Alps from 1984 to 2010: evaluation by remote sensing and
795 modeling of the morpho-topographic and climate controls, The Cryosphere, 7(5), 1455–
796 1471, doi:10.5194/tc-7-1455-2013, 2013.

797 Rabatel, A., Dedieu, J. P. and Vincent, C.: Spatio-temporal changes in glacier-wide mass
798 balance quantified by optical remote sensing on 30 glaciers in the French Alps for the
799 period 1983–2014, J. Glaciol., 62(236), 1153–1166, doi:10.1017/jog.2016.113, 2016.

800 Rabatel, A., Sirguey, P., Drolon, V., Maisongrande, P., Arnaud, Y., Berthier, E., Davaze, L.,
801 Dedieu, J.-P. and Dumont, M.: Annual and Seasonal Glacier-Wide Surface Mass Balance
802 Quantified from Changes in Glacier Surface State: A Review on Existing Methods Using
803 Optical Satellite Imagery, Remote Sens., 9(5), 507, doi:10.3390/rs9050507, 2017.

804 Racoviteanu, A. E., Williams, M. W. and Barry, R. G.: Optical Remote Sensing of Glacier
805 Characteristics: A Review with Focus on the Himalaya, Sensors, 8(5), 3355–3383,
806 doi:10.3390/s8053355, 2008.

807 Ragettli, S., Bolch, T. and Pellicciotti, F.: Heterogeneous glacier thinning patterns over the
808 last 40 years in Langtang Himal, Nepal, The Cryosphere, 10(5), 2075–2097,
809 doi:10.5194/tc-10-2075-2016, 2016.

810 Shea, J. M., Menounos, B., Moore, R. D. and Tennant, C.: An approach to derive regional
811 snow lines and glacier mass change from MODIS imagery, western North America, The
812 Cryosphere, 7(2), 667–680, doi:10.5194/tc-7-667-2013, 2013.

813 Shean, D. E., Alexandrov, O., Moratto, Z. M., Smith, B. E., Joughin, I. R., Porter, C. and Morin,
814 P.: An automated, open-source pipeline for mass production of digital elevation models
815 (DEMs) from very-high-resolution commercial stereo satellite imagery, ISPRS J.
816 Photogramm. Remote Sens., 116, 101–117, doi:10.1016/j.isprsjprs.2016.03.012, 2016.

817 Sirguey, P.: Simple correction of multiple reflection effects in rugged terrain, Int. J.
818 Remote Sens., 30(4), 1075–1081, doi:10.1080/01431160802348101, 2009.

819 Sirguey, P., Mathieu, R., Arnaud, Y., Khan, M. M. and Chanussot, J.: Improving MODIS
820 Spatial Resolution for Snow Mapping Using Wavelet Fusion and ARSIS Concept, IEEE
821 Geosci. Remote Sens. Lett., 5(1), 78–82, doi:10.1109/LGRS.2007.908884, 2008.

822 Sirguey, P., Mathieu, R. and Arnaud, Y.: Subpixel monitoring of the seasonal snow cover
823 with MODIS at 250 m spatial resolution in the Southern Alps of New Zealand:
824 Methodology and accuracy assessment, Remote Sens. Environ., 113(1), 160–181,
825 doi:10.1016/j.rse.2008.09.008, 2009.

826 Sirguey, P., Still, H., Cullen, N. J., Dumont, M., Arnaud, Y. and Conway, J. P.: Reconstructing
827 the mass balance of Brewster Glacier, New Zealand, using MODIS-derived glacier-wide
828 albedo, The Cryosphere, 10(5), 2465–2484, doi:10.5194/tc-10-2465-2016, 2016.

Six, D., Wagnon, P., Sicart, J. E. and Vincent, C.: Meteorological controls on snow and ice ablation for two contrasting months on Glacier de Saint-Sorlin, France, Ann. Glaciol., 50(50), 66–72, doi:10.3189/172756409787769537, 2009.

Sorg, A., Bolch, T., Stoffel, M., Solomina, O. and Beniston, M.: Climate change impacts on glaciers and runoff in Tien Shan (Central Asia), Nat. Clim. Change, 2(10), 725–731, doi:10.1038/nclimate1592, 2012.

Soruco, A., Vincent, C., Rabatel, A., Francou, B., Thibert, E., Sicart, J.-E. and Condom, T.: Contribution of glacier runoff to water resources of La Paz city, Bolivia (16 degrees S), Ann. Glaciol., 56(70), 147–154, doi:10.3189/2015AoG70A001, 2015.

Stocker, T., Qin, D., Plattner, G., Tignor, M., Allen, S., Boschung, J., Nauels, A., Xia, Y., Bex, B. and Midgley, B.: IPCC, 2013: climate change 2013: the physical science basis. Contribution of working group I to the fifth assessment report of the intergovernmental panel on climate change, 2013.

Van As, D.: Warming, glacier melt and surface energy budget from weather station observations in the Melville Bay region of northwest Greenland, J. Glaciol., 57(202), 208–220, doi:10.3189/002214311796405898, 2011.

Wang, W., Zender, C. S., van As, D., Smeets, P. C. J. P. and van den Broeke, M. R.: A Retrospective, Iterative, Geometry-Based (RIGB) tilt-correction method for radiation observed by automatic weather stations on snow-covered surfaces: application to Greenland, The Cryosphere, 10(2), 727–741, doi:10.5194/tc-10-727-2016, 2016.

Wolfe, R. E., Roy, D. P. and Vermote, E.: MODIS land data storage, gridding, and compositing methodology: Level 2 grid, IEEE Trans. Geosci. Remote Sens., 36(4), 1324–1338, doi:10.1109/36.701082, 1998.

Zemp, M., Frey, H., Gärtner-Roer, I., Nussbaumer, S. U., Hoelzle, M., Paul, F., Haeberli, W., Denzinger, F., Ahlstrøm, A. P., Anderson, B., Bajracharya, S., Baroni, C., Braun, L. N., Cáceres, B. E., Casassa, G., Cobos, G., Dávila, L. R., Delgado Granados, H., Demuth, M. N., Espizua, L., Fischer, A., Fujita, K., Gadek, B., Ghazanfar, A., Hagen, J. O., Holmlund, P., Karimi, N., Li, Z., Pelto, M., Pitte, P., Popovnin, V. V., Portocarrero, C. A., Prinz, R., Sangewar, C. V., Severskiy, I., Sigurðsson, O., Soruco, A., Usubaliev, R. and Vincent, C.: Historically unprecedented global glacier decline in the early 21st century, J. Glaciol., 61(228), 745–762, doi:10.3189/2015JoG15J017, 2015.